Measuring the Total Photon Economy of Molecular Species through Fluorescent Optical Cycling (FOC)

Anthony V. Sica,§ Ash Sueh Hua,§ Belle Coffey, Kierstyn P. Anderson, Benjamin T. Nguyen, Alexander M. Spokoyny, and Justin R. Caram*

Department of Chemistry and Biochemistry, University of California, Los Angeles, 607 Charles E. Young Drive, Los Angeles, California 90095-1569, USA

Abstract

The total photon economy of a molecule/material is a measure of how light input is converted to light and heat output across energies and timescales. We describe a technique, Fluorescent Optical Cycling (FOC), which allows for simultaneous observation of prompt and delayed emission *during* and *after* multiple pulsed excitation, ultimately granting access to multi-state photophysical rates. We exercise control over the excitation pulse train, which allows us to "optically shelve" long-lived intermediate states without the use of diode or flashlamp excitation. By recording all photon arrival times in the visible and shortwave infrared, we can simultaneously resolve fluorescence, phosphorescence, and singlet oxygen sensitization in a single experiment. We use FOC to examine the photophysics of dual emitting bis(di-R-phosphino)alkanethiophene-pyridine-platinum ($[Pt(thpy)(dppm)]^+$) under different solvation conditions, revealing changes in intersystem crossing and phosphorescent rates induced by the external heavy atom effect. Coupling FOC with Decay Associated Fourier Spectroscopy (DAFS), we demonstrate simultaneous correlated spectral and lifetime data in this dual emitting complex. Finally, FOC combined with superconducting nanowire single photon detectors (SNSPDs) allows us to observe the shortwave infrared region (SWIR) phosphorescence of singlet oxygen sensitized by Rose Bengal. Overall, FOC provides a

powerful tool to simultaneously study multiple photophysics across timescales, even in weakly populated electronic states.

Introduction

The total photon economy of a material represents how energy is partitioned and ultimately dissipated upon an initial excitation. Resolving the time and frequency of light emission upon excitation provides an indirect method to observe excited state dynamics through standard time-correlated single photon counting (TCSPC). However, excited state processes in materials span many orders of magnitude in time, from femtosecond vibrational coherences to seconds of delayed emission.[1] Often, the most chemically relevant excited states (e.g., those long-lived enough to participate in diffusion limited chemical reactions) may only populate once after hundreds of excitations and, even then, emit photons sparingly. Measuring long-lived emission in a time-resolved fashion limits the time resolution for shorter photophysical events because the excitation used requires long and intense illumination, such as flash lamps or LEDS. Conversely, other methods, such as transient absorption, can simultaneously resolve timescales of shorter and longer photophysical events but require high power lasers and long-delay lines. These methods lack the simple setup, low-intensity excitation, and insensitivity to scatter provided by TCSPC.[2]

We present Fluorescent Optical Cycling (FOC), a method that allows us to simultaneously study both instantaneous and delayed emissions in a material using multiple pulsed excitation as an alternative to high power excitation. Drawing from prior multiple excitation strategies for studying multi-excitons/trap states in quantum dots,[3] phosphorescent dyes,[4] and charging in perovskites,[5] we introduce tunable timed excitation pulse trains while retaining high time resolution to study the formation and decay of multiple excited states. The burst times of the pulse trains can span nanoseconds to seconds while the off time of the pulse trains can span microseconds to seconds.

Our method takes advantage of these tunable pulse trains to build population in long-lived states by 'optically shelving' via excitation over multiple pulses. We further reveal how short-time dynamics and fluorescence intensities change upon multiple excitations, providing a complementary signature that describes intersystem crossing. We implement FOC on a variety of systems, probing the features of singlet and triplet state emission. Pairing FOC with a Mach-Zehnder interferometer, we apply our previously established technique, Decay Associated Fourier Spectroscopy (DAFS), to a dual emitting system.[6] DAFS combined with FOC offers the distinguishable spectral character of prompt and delayed emission. Finally, FOC is implemented to study emissive events in the visible and shortwave infrared (SWIR, 1-2 μm) range of emission using superconducting nanowire single photon emitters (SNSPDs). FOC in the SWIR yielded the direct detection of singlet oxygen sensitized by Rose Bengal without the use of flash-lamp or continuous excitation.

Generating pulse trains with controllable off times: A pulsed laser driver (PicoQuant, PDL 800D) controls the laser repetition rate and corresponding analog synchronization signal, both of which derive from the laser driver's internal 80 MHz crystal oscillator. The sync signal from the laser driver is the global clock and is connected to the sync input channel of the TCSPC module (PicoQuant, HydraHarp 400). After amplification from a NIM to TTL converter (Micro Photon Devices, NIM 2 TTL Converter), the sync signal also triggers the delay generator (Stanford Research System, DG535). Subsequently, the delay generator output signal fast gates the laser driver, controlling both the duration of the pulsed excitation and the pulse train cycle time. The delay generator signal is also sent to the TCSPC module's marker channel to time-tag the pulse train cycle times. The delay generator is phase-locked to the TCSPC module and share the same

internal reference clock. This scheme and key electronic outputs are shown in Figure 1a. In short, the delay generator allows us to control both the number of pulses and the subsequent waiting period or laser off time. The low timing jitter of the involved electronics ensures the fidelity of the pulse trains while the high time resolution of the delay generator allows for precise control in the

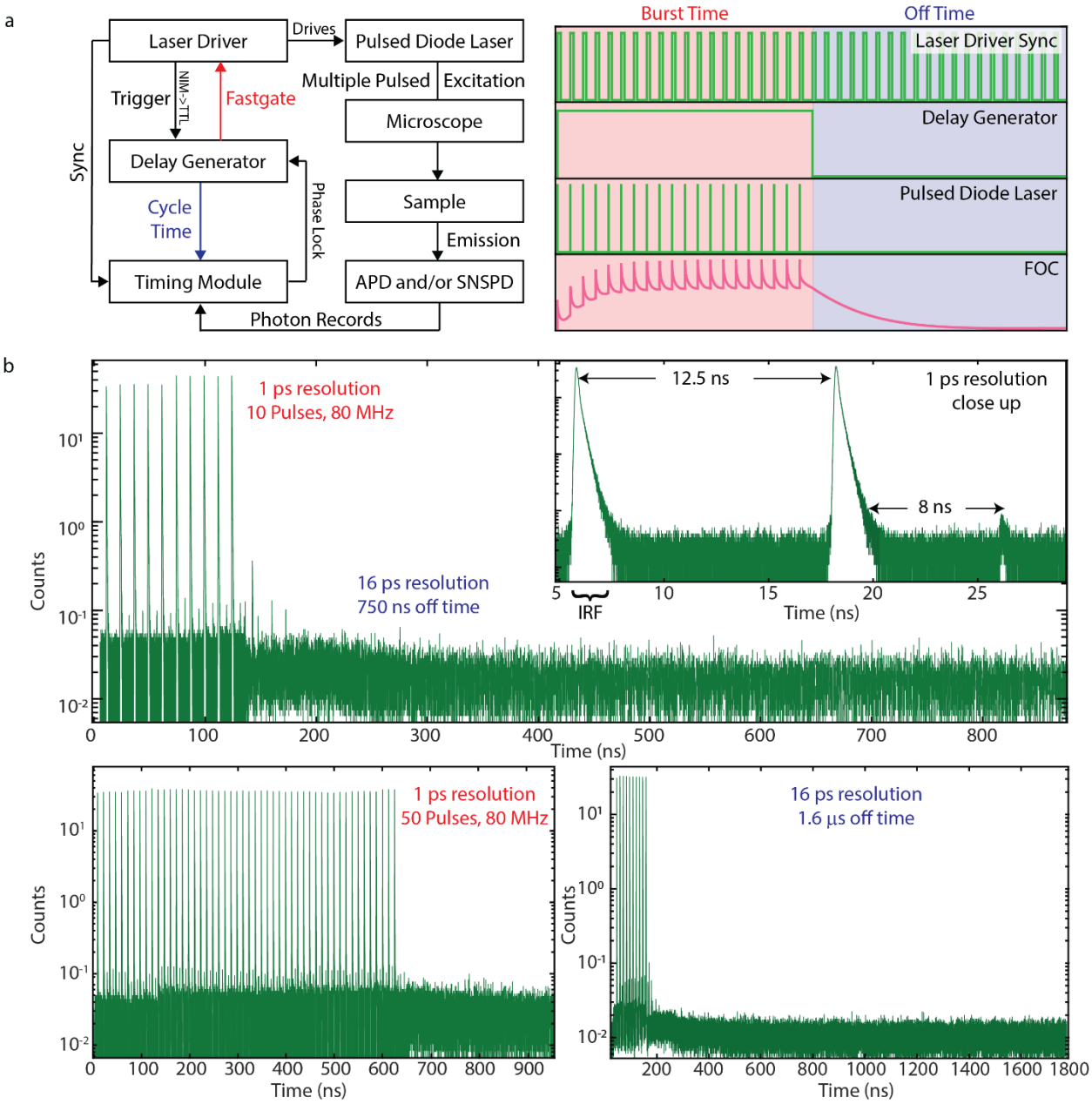

Figure 1. (a) Scheme for pulse train generation and FOC collection. The laser repetition rate triggers the delay generator, which creates a fast-gating pulse for the laser driver, ultimately controlling the burst time/number of pulses and off time. All relevant timing signals are recorded by the timing module (b) FOC trace of the instrument response function shows timing tunability of burst times/number of pulses and off times. The resolution is limited by timing module hardware and not by jitter between pulse trains.

number of laser pulses (Table S1). In Figure 1b, we show TCSPC traces of incoming laser scatter from a 532 nm pulsed diode laser (PicoQuant, LDH-P-FA-530B) to demonstrate that the number of pulses is finely controlled and that the jitter between pulse trains is less than the width of the instrument response function.

Collecting Lifetimes and FOC: Experiments were conducted on a home-built optical epifluorescence microscope, which allows for re-excitation of a small focal volume. All samples were excited by either a 532 or 405 nm pulsed diode laser (PicoQuant, LDH-P-FA-530B or LDH-P-C-405, respectively). The emission of solid-state samples was collected using a 40x air objective (Nikon, MRD00405), while the emission of solution-phase samples was collected using a 60x IR water immersion objective (Nikon, MRD07650) to ensure a tighter focal volume and higher collection efficiency through index matching. The emission was directed through our previously reported Mach-Zehnder interferometer.[6,7] The two outputs were either focused onto avalanche photodiodes (APDs) (Micro Photon Devices, PD050-CTD) for visible detection or super-conducting nanowire single photon detectors (Quantum Opus, Opus One) for NIR and SWIR detection. Complete collection of photon streams was achieved through recording in time-tagged time resolved (TTTR) mode. To prevent excitation into higher energy singlet states, laser repetition rates were selected so that the singlet excited state decays completely. Likewise, off times were selected to allow for total relaxation into the ground state, resetting the system for the next pulse train.

Modeling: To understand the results, we employ a kinetic model that is used for fitting and interpretation of the FOC signal (Figure 2a). We use a simple three-state system to model ground (S_0), singlet excited (S_1), and triplet excited state populations (T_1). Included in this model are rates for fluorescence, phosphorescence, intersystem crossing (ISC), and reverse intersystem crossing

($k_f, k_p, k_{ISC}, k_{rISC}$, respectively). Here, fluorescence and phosphorescence (k_f and k_p) are the combined radiative and non-radiative rates that connect S_1 and T_1 to the ground state (S_0). Intersystem crossing (k_{ISC}) is defined as the energy transfer from the singlet excited state to the triplet excited state, while reverse intersystem crossing (k_{rISC}) is the inverse process. Each laser pulse moves a percentage of population from the ground state to the singlet excited state, reflecting a fixed per molecule cross-section at the excitation energy. Between every pulse, the kinetics of each state are described with the following differential equations:

$$\frac{\partial[S_0]}{\partial t} = k_p[T_1] + k_f[S_1] \tag{1}$$

$$\frac{\partial[S_1]}{\partial t} = k_{rISC}[T_1] - (k_f + k_{ISC})[S_1] \tag{2}$$

$$\frac{\partial[T_1]}{\partial t} = -\left(k_p + k_{rISC}\right)[T_1] + k_{ISC}[S_1] \tag{3}$$

The solutions to the differential equations take the form of

$$[S_1] = C_{(+),S_1} \exp\left(r_{(+)}t\right) + C_{(-),S_1} \exp\left(r_{(-)}\mathrm{t}\right) \tag{4}$$

$$[T_1] = C_{(+),T_1} \exp\left(r_{(+)}t\right) + C_{(-),T_1} \exp\left(r_{(-)}\mathrm{t}\right) \tag{5}$$

Where D, $r_{(\pm)}$, $C_{(\pm),S_1}$, and $C_{(\pm),T_1}$ are as follows.

$$D = \left(k_{ISC} + k_{rISC} + k_f + k_p\right)^2 - 4(k_{ISC}k_p + k_{rISC}k_f + k_f k_p) \tag{6}$$

$$r_{(\pm)} = \frac{-\left(k_{ISC} + k_{rISC} + k_f + k_p\right) \pm \sqrt{D}}{2} \tag{7}$$

$$C_{(\pm),S_1} = \frac{1}{2\sqrt{D}}\left\{[S_1]_i\left[\mp\left(k_{ISC} - k_{rISC} + k_f - k_p\right) + \sqrt{D}\right] \pm 2k_{rISC}[T_1]_i\right\} \tag{8}$$

$$C_{(\pm),T_1} = \frac{1}{2\sqrt{D}}\left\{[T_1]_i\left[\left(k_{ISC} - k_{rISC} + k_f - k_p\right) \pm \sqrt{D}\right] \pm 2k_{ISC}[S_1]_i\right\} \quad (9)$$

The initial singlet excited and triplet excited populations at the start of every pulse number, i, are $[S_1]_i$ and $[T_1]_i$ respectively. For simplicity, implementations of this kinetic model assume reverse intersystem crossing, k_{ISC}, as negligent and set to zero. The more detailed derivation is included in the supporting information.

An example of how each of these parameters affect the FOC trace is described in Figure 2. All parameters used are included in Table S2 of the supporting information. A higher intersystem crossing rate (k_{ISC}) leads to a faster triplet buildup and a higher triplet equilibrium plateau, corresponding to a faster rate of triplet population and a larger steady-state triplet population (Figure 2b). A higher phosphorescence rate (k_p) leads to slower triplet build up and a lower triplet plateau, corresponding to a slower rate of triplet population and a smaller steady-state triplet population (Figure 2c). When more emitters are excited per pulse, we observe faster triplet buildup but an identical triplet equilibrium plateau that corresponds to a faster rate of triplet population and identical steady-state triplet population (Figure 2d). Finally, when we add a 4th pathway that depletes the triplet population, we observe two effects (Figure 2e). When depletion rates are increased, the triplet build up time is increased and the triplet equilibrium plateau is lower, signifying a slower rate of triplet population and a smaller steady-state triplet population. Simultaneously, we observe a decrease in our total signal due to a lower triplet population. The fluorescence intensities are nearly unaffected by this fourth depletion pathway.

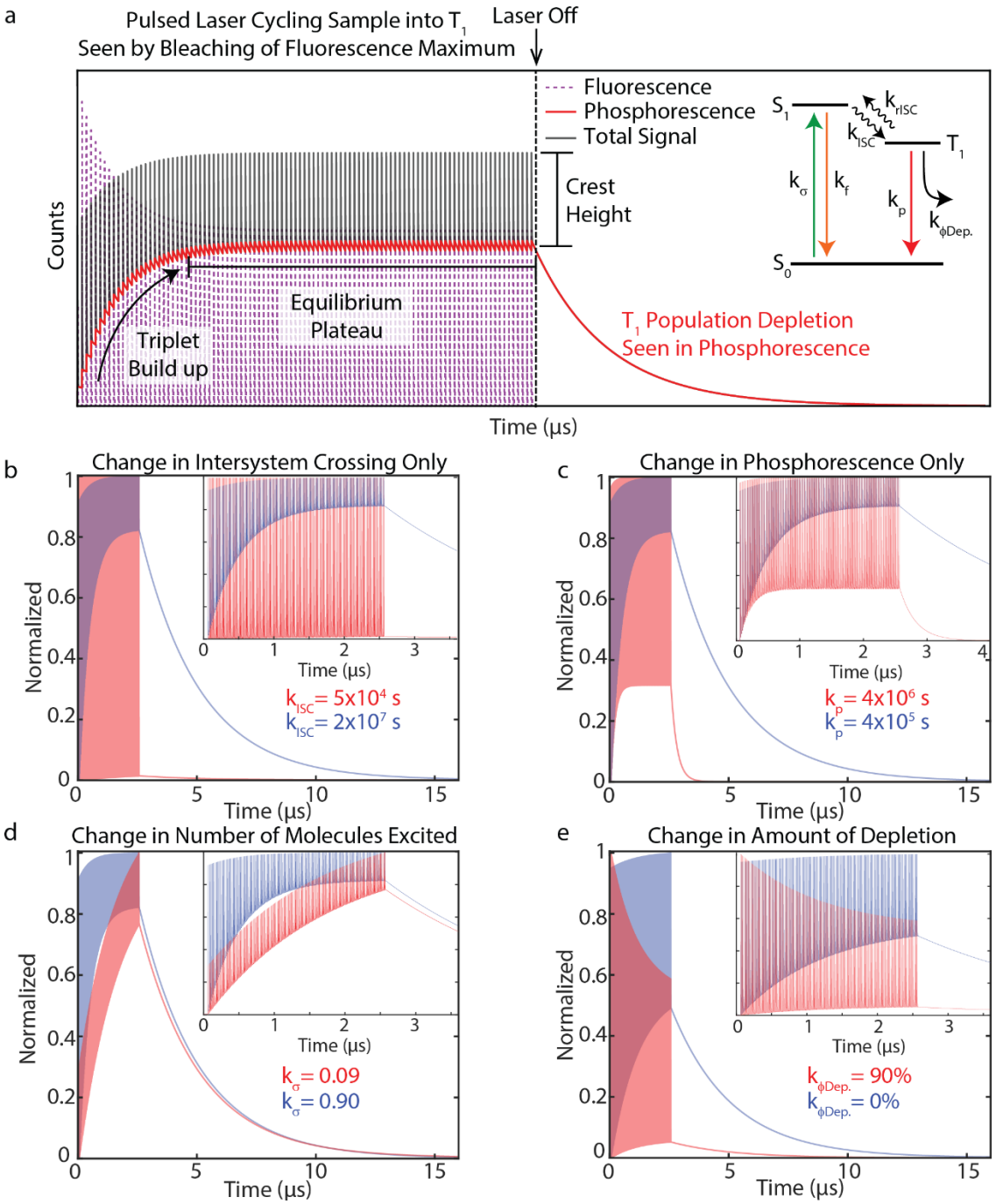

Figure 2. Demonstrating the effects of adjusting photophysical rates in the kinetic modeling derived FOC traces. (a) An FOC trace showing relative fluorescence (purple), phosphorescence (red), and total signal (grey). The decline in fluorescence amplitude/crest height is attributed to fluorescence bleaching from a significant triplet population. In the underlying phosphorescent plateau, the steep region at the beginning of the pulse train corresponds to triplet build up while the later equilibrium plateau corresponds to a steady-state triplet population. (b) A faster intersystem crossing rate leads to a faster triplet build up and a higher triplet equilibrium plateau/larger triplet population. (c) A faster phosphorescent rate leads to slower triplet build up and a lower triplet equilibrium plateau/smaller triplet population. (d) Addressing a higher percentage of emitters leads to faster triplet build up but the same height triplet equilibrium plateau. (e) A fourth decay rate from the triplet excited state leads to slower overall triplet buildup, a lower triplet equilibrium plateau height, and a sharp decrease in the total signal.

Dual Emitting Platinum Complex: We demonstrate FOC on a platinum complex, (1,1-bis(diphenylphosphino)methane)-2-(2-thienyl-κ-*3*-*C*)pyridine-κ,*N* platinum) ([Pt(thpy)(dppm)]$^+$), that exhibits simultaneous fluorescence and phosphorescence (Figure 3a). [Pt(thpy)(dppm)]$^+$ was synthesized using a procedure established by *Li, et al.*[8] where dppm ligand (dppm=1,1-bis(diphenylphosphino)methane) (1 equiv.) was added to a solution of [Pt(thpy)(Hthpy)Cl] (1 equiv.) in acetonitrile and refluxed under N_2 atmosphere. Upon isolation, [Pt(thpy)(dppm)]$^+$ was then dissolved in varying solvent ratios of diiodomethane (DIM) to dichloromethane (DCM) to induce an external heavy atom effect (EHAE) that modulates the relative amount of fluorescence to phosphorescence. With an increase in DIM, we observe a decrease in total photoluminescence (Figure S1), but also a clear increase of relative phosphorescent yield (~550-650 nm) in the emission spectra (Figure 3b). The emission spectra were normalized to the fluorescent peak (~460 nm) to emphasize this effect. Details and characterization (^{1}HNMR, UV-vis absorption and emission, and lifetimes) are provided in the SI.

The complexes were excited using a 405 nm laser diode at 10 MHz with a burst time of 10 μs and an off time of 35 μs. The total collected data is shown in (Figure 3c). We then split the resulting emission between two detectors, and use filters to isolate fluorescence in one detector and phosphorescence in the other (Figure 3d). The fluorescence FOC trace contains multiple short-lived fluorescence decays from the pulse train but not the underlying plateau attributed to phosphorescence from optical shelving into the triplet excited state. Conversely, the phosphorescence FOC trace consists of the phosphorescent plateau without multiple fluorescence decays during the burst time and a long-lived phosphorescent decay during the off time. A further proof of principle was demonstrated with highly phosphorescent boron clusters in the SI.[9]

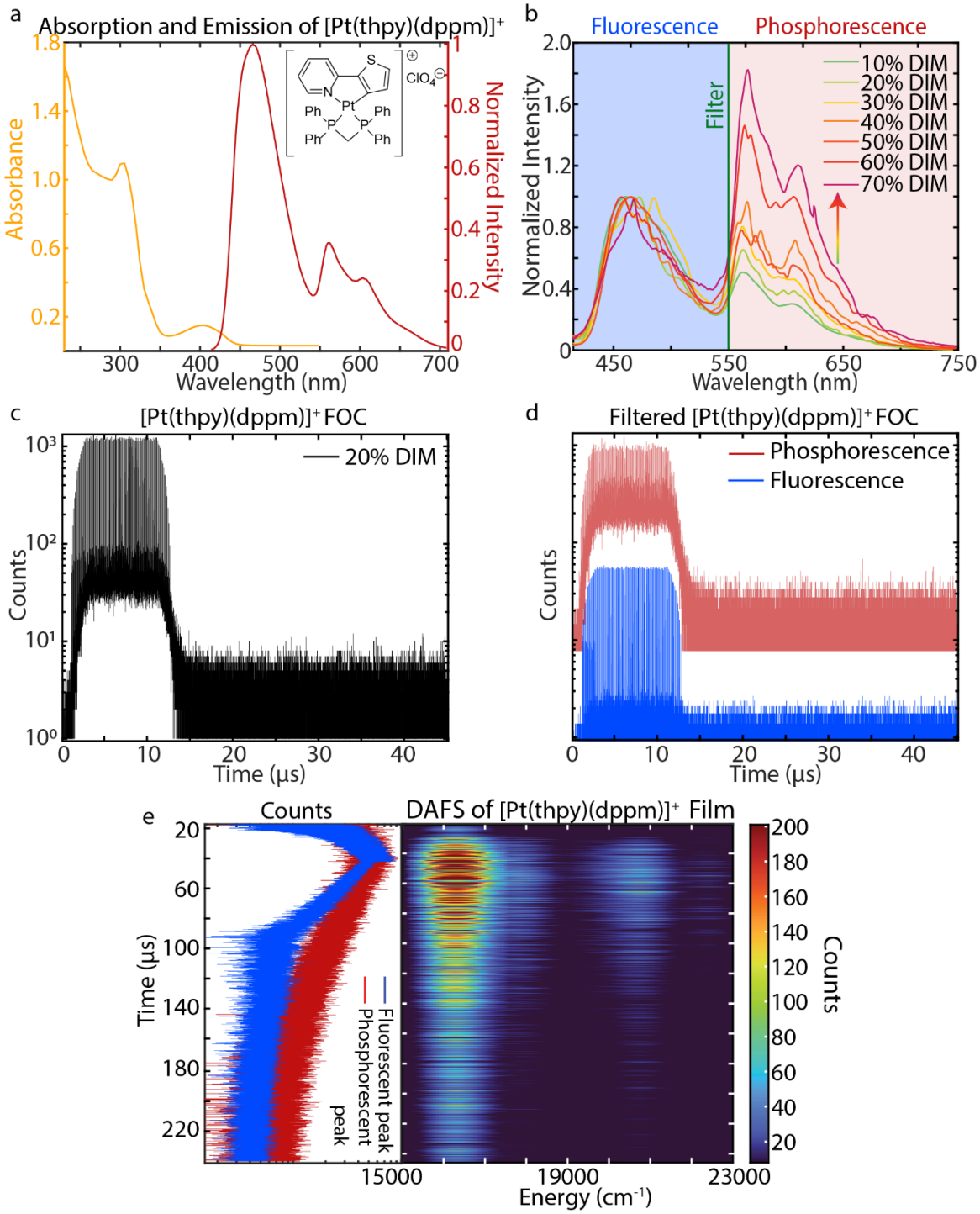

Figure 3. (a) $[Pt(thpy)(dppm)]^+$ absorption and emission in DCM. (b) $[Pt(thpy)(dppm)]^+$ emission spectra in varying solvent ratios of DIM:DCM. As the percentage of DIM increases, there is an overall increase in the relative size of the phosphorescent peak. Emission spectra were normalized to the fluorescent peak at ~460 nm. (c) FOC of $[Pt(thpy)(dppm)]^+$ in 20% DIM:DCM. (d) FOC of $[Pt(thpy)(dppm)]^+$ using dichroic filters to isolate fluorescence and phosphorescence. The phosphorescent FOC contains the characteristic plateau during the burst time and long-lived decay during the off time while the fluorescent FOC contains multiple short-lived decays from multiple pulsed excitation. (e) FOC-DAFS of 2% wt. $[Pt(thpy)(dppm)]^+$ in PMMA film. There is a clear separation of a shorter lifetime seen at the fluorescent peak while a longer lifetime is observed when integrating along the redder phosphorescent region.

FOC-DAFS of [Pt(thpy)(dppm)]$^+$: In prior work, we have used a Mach-Zehnder (MZ) interferometer to capture correlated emission and lifetime spectra.[6] Decay associated Fourier spectroscopy (DAFS) is a wavelength agnostic technique that allows octave spanning across the visible and SWIR regions. Other advantages of DAFS are optical mode retention, path-length dependent resolution, and balanced detection that allows for Fourier filtering of different fluorescent emitters.[7] To summarize, the emission is sent through a folded Mach-Zehnder interferometer where one path is varied, ultimately yielding two output beams. DAFS was used in tandem with FOC to obtain spectra correlated FOC traces of the [Pt(thpy)(dppm)]$^+$ in PMMA film (Figure 3e). The resulting DAFS displayed the photoluminescence of the [Pt(thpy)(dppm)]$^+$ with corresponding lifetimes. The complex showed a clear separation of the fluorescent and phosphorescent emissions, with phosphorescent lifetimes greatly exceeding fluorescent lifetimes.

Total Photophysics of [Pt(thpy)(dppm)]$^+$ from FOC and QY Measurements: The external heavy atom effect is observed in the total emissive quantum yield and in the relative quantum yields of fluorescence and phosphorescence (Figure 4a). As the DIM:DCM ratio is increased, the relative phosphorescence quantum yield increases compared to the relative fluorescence quantum yield. However, the total emissive quantum yield decreases with an increasing DIM:DCM solvent ratio. Collecting FOC traces at different DIM:DCM solvent ratios shows changes in the photophysical rates caused by the EHAE from DIM (Figure 4c). By fitting experimental FOC traces to the kinetic model, fluorescence, phosphorescence, and most importantly intersystem crossing can be obtained (Figure 4d).

With the addition of quantum yield measurements, the radiative decay rates can be distinguished from non-radiative decay rates since FOC only yields total fluorescence and phosphorescence

rates. The relative nonradiative rates of fluorescence and phosphorescence were found using the following equations:

$$\Phi_{rf} = \frac{k_{rf}}{k_{rf} + k_{nrf} + k_{ISC}} \tag{10}$$

$$\Phi_{ISC}\Phi_{rp} = \frac{k_{ISC}}{k_{rf} + k_{nrf} + k_{ISC}} \times \frac{k_{rp}}{k_{rp} + k_{nrp} + k_{rISC}} \tag{11}$$

Where Φ_{rf} and $\Phi_{ISC}\Phi_{rp}$ are the quantum yields of radiative fluorescence and radiative phosphorescence respectively, as measured in the emission spectra. The intersystem crossing rate and phosphorescent rate, k_{ISC} and $k_p = k_{rp} + k_{nrp}$ respectively, is found from fitting to the model, and the fluorescent rate, $k_f = k_{rf} + k_{nr}$, is from the lifetime fitting.

As the DIM:DCM ratio increases, the nonradiative fluorescent rate, k_{nrf}, remains constant while the radiative fluorescent rate, k_{rf}, decreases and the intersystem crossing rate, k_{ISC}, linearly increases (Figure 4e). As the DIM ratio increases, the intersystem crossing rate, k_{ISC}, linearly increases while the radiative phosphorescent rate, k_{rp}, decreases and the nonradiative phosphorescence, k_{nrp}, increases and decreases (Figure 4f). Interestingly, an increasing DIM solvent ratio drastically decreases both the radiative fluorescence and radiative phosphorescence rates while the both non radiative rates remain about constant; this is consistent with an increasing DIM ratio leading to decreasing emissive quantum yields. Simultaneously, increased intersystem crossing rates in conjunction with a decreased radiative fluorescence rate results in more phosphorescence emission relative to fluorescence emission with the addition of DIM.

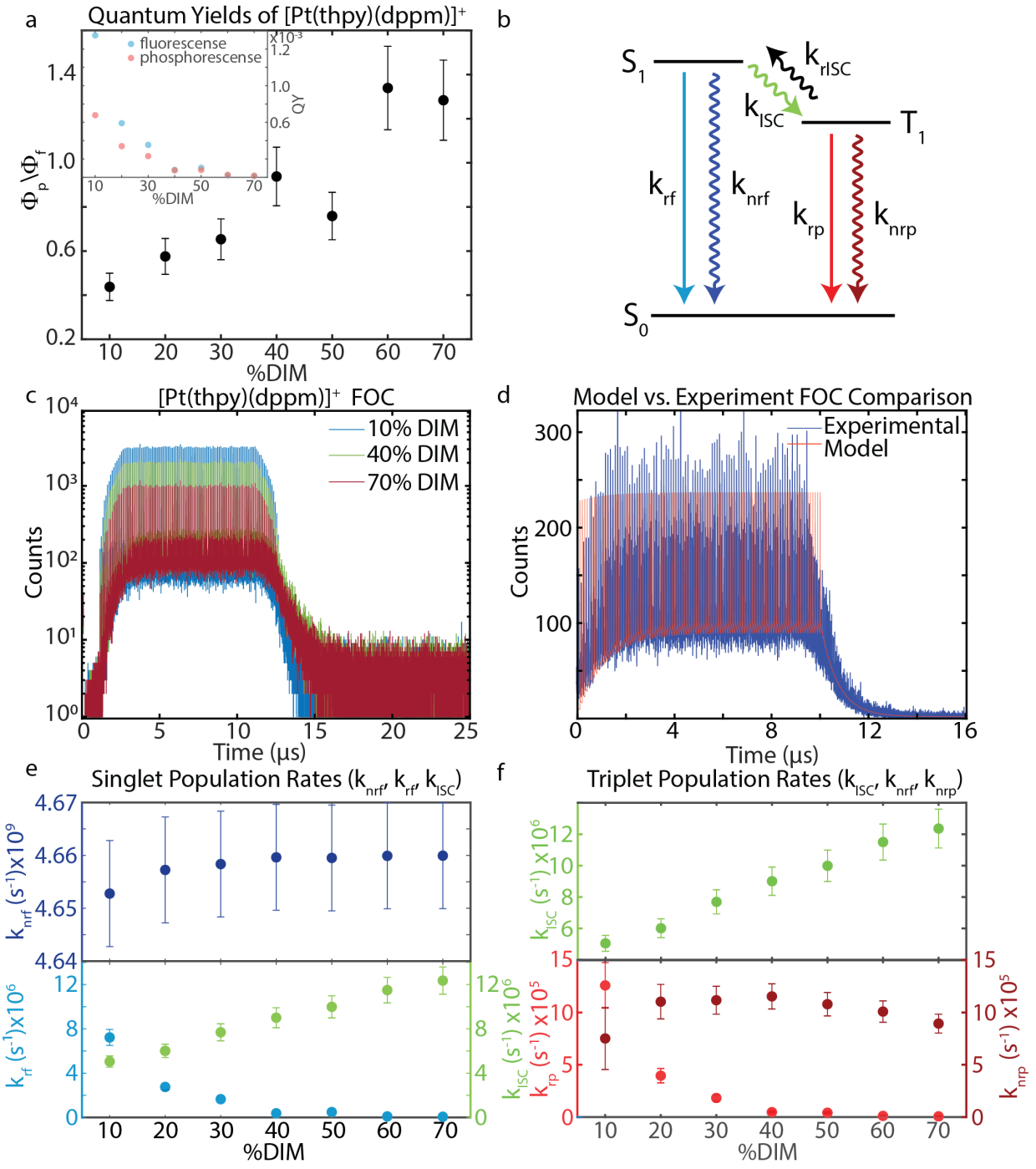

Figure 4. (a) The ratio of phosphorescent quantum yield to fluorescence quantum yield increases as the DIM solvent ratio increases. Inset: Overall emissive quantum yield decreases as the DIM solvent ratio increases. (b) Simple Jablonski with non-radiative and radiative pathways indicated. (c) $[Pt(thpy)(dppm)]^+$ FOCs in varying DIM:DCM ratios from 10% to 70% show how the DIM solvent ratio modulates photophysical rates. (d) Experimental FOC traces are fit to the kinetic model, showing good agreement. (e) Using the quantum yields and rates from FOC fitting, the nonradiative rates can be inferred. As the DIM ratio increases, the nonradiative fluorescent rate, k_{nrf}, remains constant while the radiative fluorescent rate, k_{rf}, decreases and the intersystem crossing rate, k_{ISC}, linearly increases. (f) As the DIM ratio increases, the intersystem crossing rate, k_{ISC}, linearly increases while the radiative phosphorescent rate, k_{rp}, decreases and the nonradiative phosphorescence, k_{nrp}, increases and decreases.

FOC for Direct Detection of Singlet Oxygen: Singlet oxygen plays a paramount role in an array of biological functions such as signaling for cell death and oxidative stress,[10] bioenergetics,[11] and cancer mechanisms.[12] Outside of natural systems, singlet oxygen is also used for treatments such as photodynamic therapy, where undesired tissue is damaged through photo-oxidative processes.[13] Oxygen usually exists in the triplet ground state ${}^3\Sigma_g^-$ (corresponding to two paired electrons in the same orbital) but can be excited into two singlet states termed ${}^1\Delta_g$ and ${}^1\Sigma_g^+$ (corresponding to two spin paired electrons in different orbitals) (Figure 5a). Ground state triplet oxygen can be sensitized to a higher excited singlet state through interaction with a sensitizing dye molecule that can undergo triplet-triplet energy transfer (Figure 5b). One method to probe singlet oxygen directly is through its phosphorescent emission from the ${}^1\Delta_g$ state at 1275 nm, in the short-wave infrared (SWIR). Superconducting nanowire single-photon detectors (SNSPDs) previously have been used to detect singlet oxygen.[14] We enhance singlet oxygen emission through FOC and study the dynamics of singlet oxygen and singlet oxygen sensitization using SNSPDs.

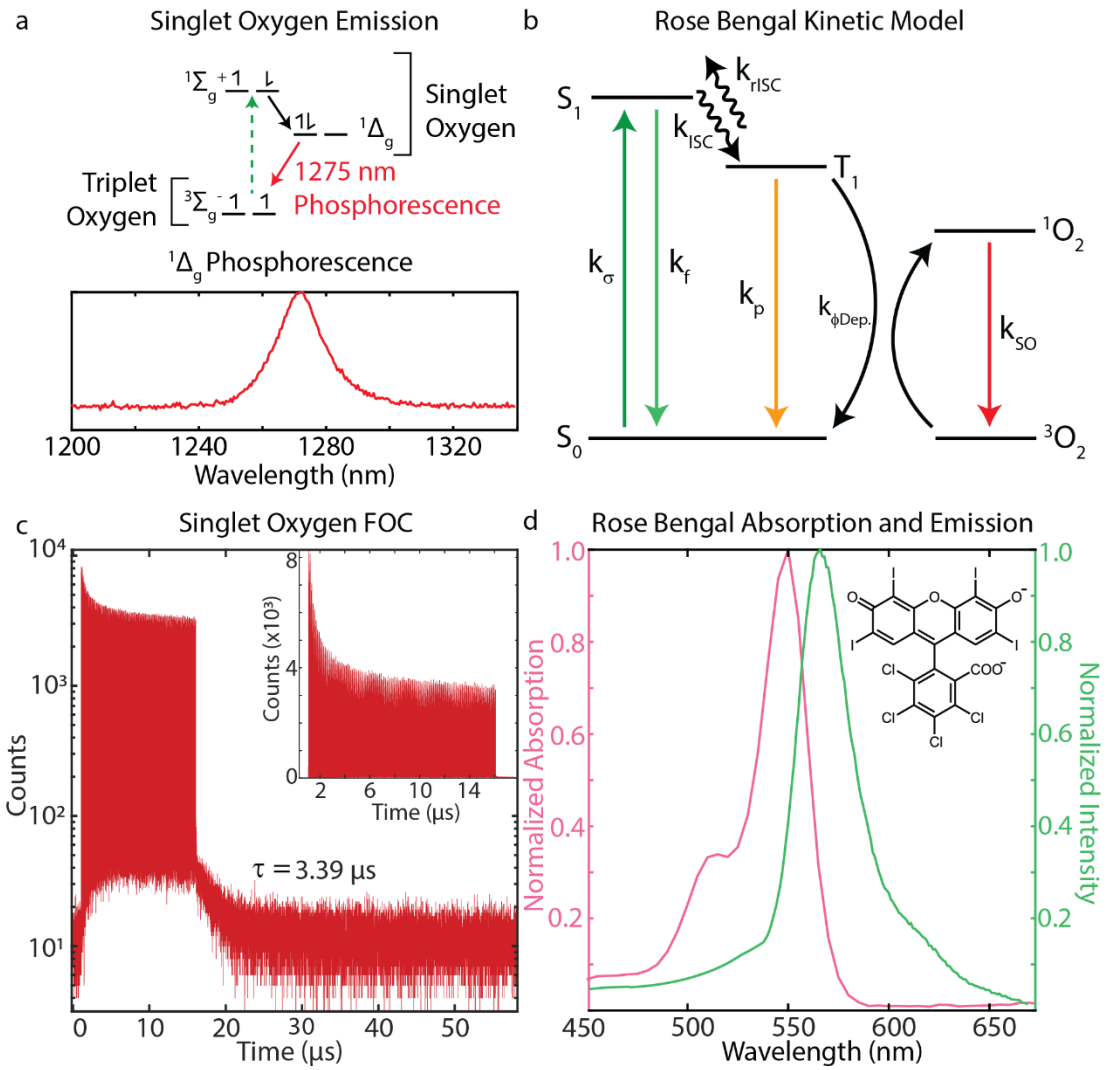

Figure 5. (a) Electronic states and emission (~1275 nm) of singlet oxygen. (b) Jablonski diagram for dye sensitization of singlet oxygen. Triplet-triplet annihilation of a triplet excited state dye with triplet ground state oxygen produces singlet excited state oxygen. (c) FOC of singlet oxygen sensitized by Rose Bengal collected with SNSPDs. The lifetime of singlet oxygen in water is 3.39 µs. (d) Absorption and emission spectra of Rose Bengal in water.

Rose Bengal, as a sensitizer for singlet oxygen, was purposely used to directly detect singlet oxygen generation at ~1275 nm. A sample of Rose Bengal in water was flowed through a perfusion cell chamber (details in the SI). Flowing the sample helped regenerate chromophores and collect emission of singlet oxygen at higher yields and in less time. The sample's emission was detected using custom broadband SNSPDs (Quantum Opus, Opus One), which boast high quantum efficiencies and fast reset times. Before collection, a 533 nm notch filter (Thorlabs, NF533-17) and 550 nm LP (Newport, 10CGA-550) were used to filter out most of the sensitizer fluorescence.

The sample was collected using a 532 nm laser at 80 MHz with a hold time of ~15 μs and an off-time of 60 μs. In this FOC, we see a gradual decrease in the total signal height during the burst time, which is emphasized in the inset linear plot (Figure 5c). This is modeled as an additional depletion event from the triplet excited state of Rose Bengal, where triplet excited state Rose Bengal undergoes triplet-triplet energy transfer with triplet ground state oxygen to produce excited state singlet oxygen. The decrease in total signal here is attributed to slower overall long-lived photoluminescent population build up, and smaller steady state long-lived photoluminescent population. This contributes to the total signal being dominated by shorter lifetime components and higher yield in nonradiative pathways. The FOC burst time begins to resemble the decrease in total signal seen in our example model (Figure 2d). When fitting the tail from the off time, the lifetime is found to be 3.39 μs and in excellent agreement with photosensitized room temperature studies which found the lifetime of singlet oxygen in water to be 3.5 μs.[15,16]

Comparison to Other Methods: In addition to the methods highlighted in the introduction that inspired this effort, we note several other methods used to extract phosphorescent rates. A recent paper uses a similar approach, burst-mode Time Gated Fourier Transform Spectroscopy (bmTG-FTS), where multiple pulsed excitation is combined with a Fourier spectroscopy method, Translating Wedge-based Identical pulses eNcoding System (TWINS), in order to obtain correlated timescale spanning spectral information.[17] It is important to note that we resolve non steady-state dynamics during multi-pulsed excitation, yielding additional rich photophysical information in the form of often neglected nonradiative rates, such as intersystem crossing rates. In addition, our implementation of FOC-DAFS possesses the advantages of DAFS, including dual detector enabled balanced detection, drift cancellation, wavelength agnostic detection, and visible

to SWIR octave spanning collection. Comparisons between DAFS and TWINS have been discussed extensively in prior literature.[6]

Jahn. et. al. presents a single pulsed excitation technique for simultaneous fluorescent lifetime imaging (FLIM) and phosphorescent lifetime imaging (PLIM) but is only feasible with the use of bright dual emitters and compromised time resolution.[18] Another technique for simultaneous FLIM/PLIM from Becker et. al. similarly leverages multi-pulsed excitation to optically shelve into triplet excited states, but ignores the non-steady state nature of multiple pulsed excitation.[19] As a result, intersystem crossing and other non-radiative rates are neglected and only averaged fluorescent lifetimes and phosphorescent lifetimes are obtained. The combination of FOC for simultaneous FLIM/PLIM is a future application that will add photophysical depth to FLIM/PLIM.

Discussion and Conclusion: We demonstrate the utility of FOC in resolving the total photophysics of an emitter by simultaneously measuring both short-lived and long-lived emission without compromising time resolution. The non-steady state measurement of both short-lived and long-lived emission allows for the extraction of often neglected photophysical parameters such as intersystem crossing rates in addition to total fluorescence and phosphorescence rates. The addition of quantum yield information allows for further interrogation of photophysical rates, where the total fluorescent and phosphorescent decay rates can be separated into radiative and nonradiative components. To our knowledge, phosphorescent nonradiative rates are not often characterized, despite potential chemical relevance in photochemistry. How these rates change as a function of solvation environment likely reflects the degree to which the solvent and coordination environment influences “parity forbidden” recombination of states.

Along these lines, we demonstrated in a dual emissive platinum complex, [Pt(thpy)(dppm)]ClO_4, that the intersystem crossing rates increase linearly with the EHAE solvent ratio. Simultaneously,

the nonradiative phosphorescent rate follows a nonlinear increase. We hypothesize this may reflect the mechanism by which EHAE affects the rates of parity forbidden decay. Linear changes may reflect direct binding of DCM/DIM to the platinum complex, while nonlinear effects suggest a more complex relationship between the coordination sphere and phosphorescent quenching. FOC may help elucidate these complications in the future. Similarly, detailed studies of the mechanism and timescales of singlet oxygen sensitization using direct observation of both the sensitizer and singlet oxygen are often quite challenging as they span energy and timescales, and rely on a weakly emissive phosphorescent signature. We believe that FOC will enable detailed spectroscopic interrogation of photosensitization for a range of applications from photodynamic therapies to oxygen mediated catalysis. Combining FOC with control over the excitation volume and other TCSPC based methods such as DAFS (for spectral access) and SNSPDs (for infrared photons) can allow us to maximally extract information encoded within the photon stream, revealing the total photon economy of an emissive system.

Acknowledgements

A.V.S., A.S.H., B.C, and J.R.C. acknowledge funding from the National Science Foundation, Career Grant (CHE-1945572), and the ACS Petroleum Research Fund (62717-DNI6). A. M. S. thanks NSF (CHE-1866849) for financial support. K. A. is grateful to NSF for a GRFP award (DGE-1650604)

References

(1) Zewail, A. Femtochemistry: Atomic-Scale Dynamics of the Chemical Bond Using Ultrafast Lasers. In *Nobel Lectures, Chemistry 1996-2000*; Grenthe, I., Ed.; World Scientific Publishing Co.: Singapore, 2003.

(2) Penzkofer, A.; Beidoun, A.; Daiber, M. Intersystem-Crossing and Excited-State Absorption in Eosin Y Solutions Determined by Picosecond Double Pulse Transient Absorption Measurements. *J Lumin* **1992**, *51* (6), 297–314. https://doi.org/10.1016/0022-2313(92)90059-I.

(3) Singh, G.; Guericke, M. A.; Song, Q.; Jones, M. A Multipulse Time-Resolved Fluorescence Method for Probing Second-Order Recombination Dynamics in Colloidal Quantum Dots. *Journal of Physical Chemistry C* **2014**, *118* (26), 14692–14702. https://doi.org/10.1021/JP5043766/SUPPL_FILE/JP5043766_SI_001.PDF.

(4) Shcheslavskiy, V. I.; Neubauer, A.; Bukowiecki, R.; Dinter, F.; Becker, W. Combined Fluorescence and Phosphorescence Lifetime Imaging. *Appl Phys Lett* **2016**, *108* (9), 091111. https://doi.org/10.1063/1.4943265.

(5) Saba, M.; Aresti, M.; Quochi, F.; Marceddu, M.; Loi, M. A.; Huang, J.; Talapin, D. V.; Mura, A.; Bongiovanni, G. Light-Induced Charged and Trap States in Colloidal Nanocrystals Detected by Variable Pulse Rate Photoluminescence Spectroscopy. *ACS Nano* **2013**, *7* (1), 229–238. https://doi.org/10.1021/NN305031K/SUPPL_FILE/NN305031K_SI_001.PDF.

(6) Atallah, T. L.; Sica, A. V.; Shin, A. J.; Friedman, H. C.; Kahrobai, Y. K.; Caram, J. R. Decay-Associated Fourier Spectroscopy: Visible to Shortwave Infrared Time-Resolved Photoluminescence Spectra. *Journal of Physical Chemistry A* **2019**, *123* (31), 6792–6798. https://doi.org/10.1021/ACS.JPCA.9B04924/ASSET/IMAGES/LARGE/JP-2019-04924T_0005.JPEG.

(7) Sica, A. V.; Hua, A. S.; Lin, H. H.; Sletten, E. M.; Atallah, T. L.; Caram, J. R. Spectrally Selective Time-Resolved Emission through Fourier-Filtering (STEF). *Journal of Physical Chemistry Letters* **2023**, *14* (2), 552–558. https://doi.org/10.1021/ACS.JPCLETT.2C01504/SUPPL_FILE/JZ2C01504_SI_002.PDF.

(8) Li, K.; Tong, G. S. M.; Yuan, J.; Ma, C.; Du, L.; Yang, C.; Kwok, W. M.; Phillips, D. L.; Che, C. M. Excitation-Wavelength-Dependent and Auxiliary-Ligand-Tuned Intersystem-Crossing Efficiency in Cyclometalated Platinum(II) Complexes: Spectroscopic and Theoretical Studies. *Inorg Chem* **2020**, *59* (20), 14654–14665. https://doi.org/10.1021/ACS.INORGCHEM.0C01192/ASSET/IMAGES/LARGE/IC0C01192_0007.JPEG.

(9) Anderson, K. P.; Hua, A. S.; Plumley, J. B.; Ready, A. D.; Rheingold, A. L.; Peng, T. L.; Djurovich, P. I.; Kerestes, C.; Snyder, N. A.; Andrews, A.; Caram, J. R.; Spokoyny, A. M. Benchmarking the Dynamic Luminescence Properties and UV Stability of B18H22-Based Materials. *Dalton Transactions* **2022**, *51* (24), 9223–9228. https://doi.org/10.1039/D2DT01225A.

(10) Laloi, C.; Havaux, M. Key Players of Singlet Oxygen-Induced Cell Death in Plants. *Front Plant Sci* **2015**, *6* (FEB), 39. https://doi.org/10.3389/FPLS.2015.00039/BIBTEX.

(11) Sokolovski, S. G.; Rafailov, E. U.; Abramov, A. Y.; Angelova, P. R. Singlet Oxygen Stimulates Mitochondrial Bioenergetics in Brain Cells. *Free Radic Biol Med* **2021**, *163*, 306–313. https://doi.org/10.1016/J.FREERADBIOMED.2020.12.022.

(12) Baier, J.; Maisch, T.; Maier, M.; Landthaler, M.; Bäumler, W. Direct Detection of Singlet Oxygen Generated by UVA Irradiation in Human Cells and Skin. *J Invest Dermatol* **2007**, *127* (6), 1498–1506. https://doi.org/10.1038/SJ.JID.5700741.

(13) Dolmans, D. E. J. G. J.; Fukumura, D.; Jain, R. K. Photodynamic Therapy for Cancer. *Nature Reviews Cancer 2003 3:5* **2003**, *3* (5), 380–387. https://doi.org/10.1038/nrc1071.

(14) Gemmell, N. R.; McCarthy, A.; Liu, B.; Tanner, M. G.; Dorenbos, S. N.; Zwiller, V.; Patterson, M. S.; Buller, G. S.; Wilson, B. C.; Hadfield, R. H. Singlet Oxygen Luminescence Detection with a Fiber-Coupled Superconducting Nanowire Single-Photon Detector. *Optics Express, Vol. 21, Issue 4, pp. 5005-5013* **2013**, *21* (4), 5005–5013. https://doi.org/10.1364/OE.21.005005.

(15) Herzberg, G.; Mrozowski, ; S. Molecular Spectra and Molecular Structure. I. Spectra of Diatomic Molecules. *Am J Phys* **1951**, *19* (6), 390–391. https://doi.org/10.1119/1.1932852.

(16) Bregnhøj, M.; Westberg, M.; Jensen, F.; Ogilby, P. R. Solvent-Dependent Singlet Oxygen Lifetimes: Temperature Effects Implicate Tunneling and Charge-Transfer Interactions. *Physical Chemistry Chemical Physics* **2016**, *18* (33), 22946–22961. https://doi.org/10.1039/C6CP01635A.

(17) Liisberg, M. B.; Rück, V.; Vosch, T. Time Gated Fourier Transform Spectroscopy with Burst Excitation for Time-Resolved Spectral Maps from the Nano- to Millisecond Range. *Chemical Communications* **2023**, *59* (84), 12625–12628. https://doi.org/10.1039/D3CC03961G.

(18) Jahn, K.; Buschmann, V.; Hille, C. Simultaneous Fluorescence and Phosphorescence Lifetime Imaging Microscopy in Living Cells. *Scientific Reports 2015 5:1* **2015**, *5* (1), 1–13. https://doi.org/10.1038/srep14334.

(19) Becker, W.; Su, B.; Bergmann, A.; Weisshart, K.; Holub Wolfgang Becker, O. Simultaneous Fluorescence and Phosphorescence Lifetime Imaging. *https://doi.org/10.1117/12.875204* **2011**, *7903* (11), 291–297. https://doi.org/10.1117/12.875204.